# Towards ultraefficient nanoscale straintronic microwave devices

Mike Jaris,[*] Weigang Yang,[*,†] Cassidy Berk, and Holger Schmidt
*School of Engineering, University of California Santa Cruz, Santa Cruz, California 95064, USA*

(Received 1 February 2019; revised manuscript received 9 December 2019; accepted 28 May 2020; published 11 June 2020)

We investigate the ultrafast magnetization dynamics of individual nanomagnets resonantly excited by surface acoustic waves (SAWs) generated nonlocally by nonmagnetic phononic gratings. Using a time-resolved magneto-optic Kerr effect microscope, we report the dependence of the magnetoelastic resonance on SAW wavelength and nanomagnet size. Our measurements show that the precession amplitude of single nanomagnets increases monotonically and nonlinearly with decreasing sample size. In addition, for nanomagnets below a critical size we find that the oscillation amplitude increases with SAW frequency. Field-swept measurements of the magnetization dynamics reveal that the damping of the magnetoelastic resonance also decreases with the size of the magnet, ultimately reaching a minimum value determined by the Gilbert damping. This work shows that acoustically driven spin dynamics possess favorable scaling characteristics, which supports the notion that efficient, high-frequency (10–100 GHz) nanoscale straintronic devices limited only by $\alpha$ are feasible.

DOI: 10.1103/PhysRevB.101.214421

## I. INTRODUCTION

As conventional building blocks for computation such as silicon-based logic gates and granular magnetic media rapidly approach fundamental physical limits that preclude further miniaturization, there is a growing need for alternative memory technologies with more favorable scaling properties [1,2]. To this end, nanostructured magnetic devices have long been identified as the leading candidates to supplant incumbent technologies thanks to their numerous, highly desirable properties [3,4]. One enticing property of nanomagnetic structures is the strong coupling between the electron spins and various degrees of freedom that make it possible to control the magnetization optically, electrically, or even acoustically [5–10]. The latter has been underexplored, but has received renewed interest in recent years thanks to improved nanofabrication capabilities that have enabled the realization of novel "straintronic" designs. Strain-mediated magnetic devices such as magnetophononic crystals [11], acoustically assisted spin transfer-torque magnetic random access memory devices [12], and most notably, ultralow-power nanomagnetic logic devices controlled by surface acoustic waves (SAWs) [13] have already been demonstrated.

Although the dynamic magnetic properties of nanoscale straintronic devices are known to directly determine critical operation characteristics, few studies [14–16] have investigated acoustically driven spin dynamics in individual nanostructures. Here, we study the SAW-driven spin dynamics of isolated nanomagnets with diameters ($D$) ranging from 730 to 150 nm excited by various SAW wavelengths ($\lambda_{SAW}$) in order to elucidate the geometric parameters that affect device performance (Fig. 1). Our results show that the amplitude of the magnetoelastic (MEL) resonance increases by more than an order of magnitude as the nanomagnet $D$ is reduced from 730 to 150 nm. In addition, we observe that the oscillation amplitude increases with SAW frequency when the nanomagnet diameter is less than a critical value. Finally, from our field-dependent measurements of the magnetoelastically driven response, we show unambiguously that the damping of the resonance depends on the nanomagnet size when $D > \lambda_{SAW}$, whereas for smaller magnets the efficiency of the MEL resonance is limited solely by $\alpha$. These results demonstrate that the performance of high-frequency, magnetoelastically controlled devices scale favorably with decreasing diameter and SAW wavelength, both of which are relevant to the design of nanoscale straintronic devices. Using a hybrid finite-element/finite-difference method magnetomechanical simulation procedure, we show that the spatial character of the SAW-driven resonance is highly non-uniform for large devices (e.g., $D > \lambda_{SAW}$) and is the origin of the enhanced damping and diminished response we observe in large magnets.

## II. EXPERIMENTAL DETAILS

Isolated nickel (Ni) nanocylinders (30 nm thick) were defined between two sets of identical, nonmagnetic aluminum (Al) bars [Fig. 1(a)] on a (100) Si substrate capped by a 110-nm-thick hafnium oxide ($HfO_2$) antireflection (AR) coating [17,18] utilizing multilevel electron-beam lithography, electron beam evaporation, and lift-off processes. The wavelength of the acoustic wave is set by the pitch $p$ of the Al wires ($\lambda_{SAW} = p$) and directly determines the frequency of the SAW ($f_{SAW}$) via the ratio $f_{SAW} = v_s/p$, where $v_s$ is the speed of sound for the SAWs. Three sets of Al bars (width = ~200 nm, thickness = ~30 nm) were fabricated with pitches of 309, 362, and 412 nm corresponding to SAW frequencies of 9.8, 8.7, and 7.8 GHz, respectively. To generate SAWs, two

[*]These authors contributed equally to this work.
[†]wyang27@ucsc.edu

 

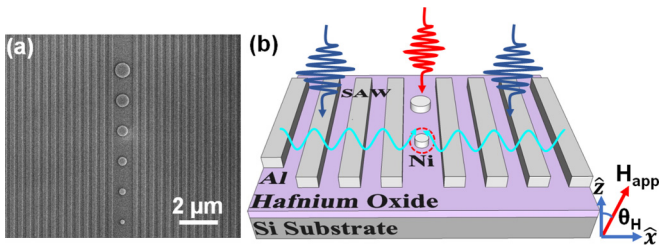


FIG. 1. (a) Scanning electron microscope image of isolated Ni nanomagnets with different sizes embedded between an Al nanowire array (pitch = 400 nm). (b) Schematic view of the MEL excitation in individual Ni nanomagnet with different sizes.

ultrafast pump pulses ($\lambda_{\text{pump}} = 400$ nm, pulse width = 150 fs, repetition rate = 76 MHz, mechanically chopped at 1 kHz) are generated by second-harmonic generation of an ultrafast Ti:sapphire laser and subsequently split using a beam splitter. The pulses are focused through a microscope objective [$M = 100\times$, numerical aperture = 0.9, full width at half maximum (FWHM) = 3.5 $\mu$m each] onto the Al bars on either side of the nanomagnets. Upon absorption, the bars undergo impulsive thermal expansion, which in turn produces a periodic elastic strain along the sample surface that launches counterpropagating SAWs into the $HfO_2$ layer towards the Ni nanomagnet, thereby forming a standing acoustic wave [Fig. 1(b)]. Knife-edge measurements were performed on both the pump and probe beams to determine their exact spatial character, and to ensure that the pump pulse did not optically excite the nanomagnet. The center of each pulse is at least 3 $\mu$m away from the nanomagnet to minimize both the photoexcitation of the spin system and the distance the SAW must travel to reach the nanomagnet. The magnetization dynamics are then recorded using the time-resolved magneto-optic Kerr effect (TR-MOKE). A mechanically delayed probe pulse [19–22] ($\lambda_{\text{probe}} = 800$ nm, pulse width = 150 fs, repetition rate = 76 MHz, FWHM = 0.58 $\mu$m) is focused onto the nanomagnet and experiences a gyrotropic polarization rotation upon reflection. Lock-in detection at the pump modulation frequency is used to record the Kerr rotation (magnetic) as well as the elastic motion (nonmagnetic) using the difference and sum signal of a balanced photodetector setup, respectively. A variable external applied field ($H_{\text{app}}$) with an in-plane component that is parallel to the propagation direction of SAWs is held at a fixed angle $\theta = 30^\circ$ from the surface normal [Fig. 1(b)].

## III. RESULTS AND DISCUSSION

To study the effect of nanomagnet size and SAW wavelength on the magnetoelastic resonance amplitude, we recorded the precessional dynamics of nanomagnets with varying diameters driven by SAWs on resonance (i.e., $H_{\text{app}} = H_{\text{res}}$), where $H_{\text{res}}$ is the external field at which the ferromagnetic resonance frequency is identical to $f_{\text{SAW}}$. Because the nanomagnets in this study are smaller than the $1/e^2$ diameter of the probe beam ($2w_0 = 1\,\mu$m), a portion of the back-reflected beam comes from the substrate and is, therefore, nonmagnetic in nature. Consequently, the polarization rotation of the back-reflected beam [$\Delta\theta_{k,m}(t)$] is inevitably smaller than the Kerr rotation [$\Delta\theta_k(t)$] of the light that interacts with the surface of the magnet. Thus, to determine the amplitude of the magnetic precession the nonmagnetic contribution needs to be accounted for. Per Ref. [17], the amplitude of the true Kerr rotation of the nanostructure can be determined via the following relation:

$$\theta_k(t) = \Delta\theta_{k,m}(t)\left(1 + \frac{R_{\text{sub}}}{R_{\text{mag}}}\frac{1}{e^{D^2/2w_0^2} - 1}\right), \tag{1}$$

where $R_{\text{sub}}$ and $R_{\text{mag}}$ are the reflectance of the substrate and Ni thin film, respectively, and $w_0$ is the beam waist of the Gaussian probe beam. In Figs. 2(a) and 2(b), Eq. (1) was used to plot the time evolution of the Kerr rotation of two nanomagnets ($D = 200$ and 730 nm, respectively) resonantly excited by SAWs. These data show that the oscillation amplitudes scale differently with $\lambda_{\text{SAW}}$ for these two nanomagnets. The maximum precession amplitudes of each sample considered in this study are summarized in Fig. 2(c), which clearly shows that $\Delta\theta_k(t)$ shrinks with increasing $D$. Moreover, we find that when $\frac{D}{\lambda_{\text{SAW}}} < 1.5$, the signal amplitude decreases as a function of nanomagnet size and is modeled well by a monoexponential decay, as shown by the dashed lines in Fig. 2(c).

For the larger samples $\left(\frac{D}{\lambda_{\text{SAW}}} > 1.5\right)$, we conjecture that dynamic dephasing of the signal due to the inhomogeneous spatial character of the resonance results in a smaller $\Delta\theta_K$. This interpretation is consistent with the mode profiles obtained from micromagnetic simulations of the MEL response that we discuss later in this paper. For small samples, as $D$ decreases the strain profile and magnetoelastic field ($H_{\text{MEL}}$) in the sample become more uniform, which results in better coupling between the phononic and magnonic systems and an exponential rise in the signal amplitude.

We now turn our attention to the damping associated with the SAW-driven magnetization precession, which can be analyzed by measuring the field-swept response of nanomagnets excited by SAWs as described in Ref. [16]. Briefly, we record the time evolution at each applied field, then convert the signal to the frequency domain using a fast Fourier transform (FFT) algorithm and combine the Fourier spectra at each applied field to produce a field-dependent colormap [Fig. 3(a)]. From the surface plot, we see that the response is only triggered at $f_{\text{SAW}}$ in the vicinity of $H_{\text{res}}$ over a range of applied fields we refer to as the "pinning width" ($\Delta H_p$), which is determined by fitting the real and imaginary parts of the Fourier spectra [Fig. 3(b)] using Lorentzian-like functions [16]. We then use $\Delta H_p$ to calculate the effective damping via the following relation:

$$\alpha_{\text{eff}}(H_{\text{app}}) = \frac{\gamma\,\Delta H_p}{4\pi f_{\text{SAW}}}. \tag{2}$$

In Fig. 3(c), we show the effective damping determined using this relationship as a function of $D$ for nanomagnets driven by the same SAW wavelength ($\lambda_{\text{SAW}} = 412$ nm). The damping of the smallest samples in this study ($D = 150$ and 200 nm) is virtually identical to the intrinsic damping ($\alpha = 0.03$) determined from conventional TR-MOKE measurements (i.e., pump-probe) on an unpatterned film. Here, we see that the effective damping of the resonance is

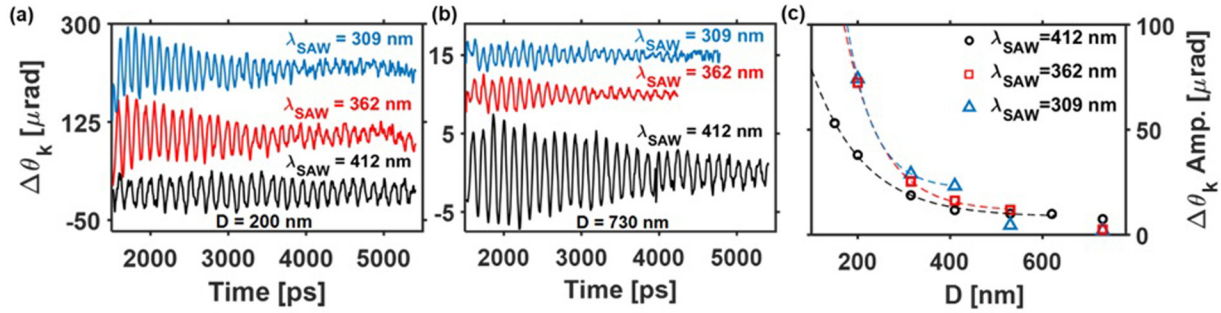


FIG. 2. SAW-driven spin dynamics for the (a) $D = 200$-nm and (b) $D = 730$-nm nanomagnets excited by three different SAW wavelengths show the distinct behavior of the two different sample sizes; the traces are offset in (a) and (b) for visualization and the rotation angle was determined using Eq. (1). In (c) the precession amplitude of each sample is plotted (symbols) to show how $\Delta\theta_K$ changes with $D$ at three different $\lambda_{SAW}$ values; the dashed lines are the results of fitting an exponential function ($\Delta\theta_k = Ae^{-\frac{D}{B}} + C$) to the data that satisfies $D < 1.5\ \lambda_{SAW}$.

essentially $\alpha$ when $D < \lambda_{SAW}$; however, for larger samples $\alpha_{eff}$ is significantly higher than the Gilbert damping. To determine whether the SAW wavelength influences the damping measurement, we carried out field-swept measurements of the $D = 200$ nm for all three SAW wavelengths [Fig. 3(d)]. In this case, the nanomagnet is always smaller than $\lambda_{SAW}$ and the linewidth of the MEL resonance corresponds to a damping value that is within error of $\alpha$. Thus, our measurements show that using SAWs to drive spin precessions in nanomagnets scales favorably with the device size, and is ultimately limited by only the Gilbert damping when the lateral dimensions are smaller than the acoustic wavelength. To put this into perspective, technologically relevant nanomagnet sizes have already reached single-nanometer length scales. Based on our observations, SAWs with wavelengths as small as tens of nanometers, which corresponds to a frequency range of

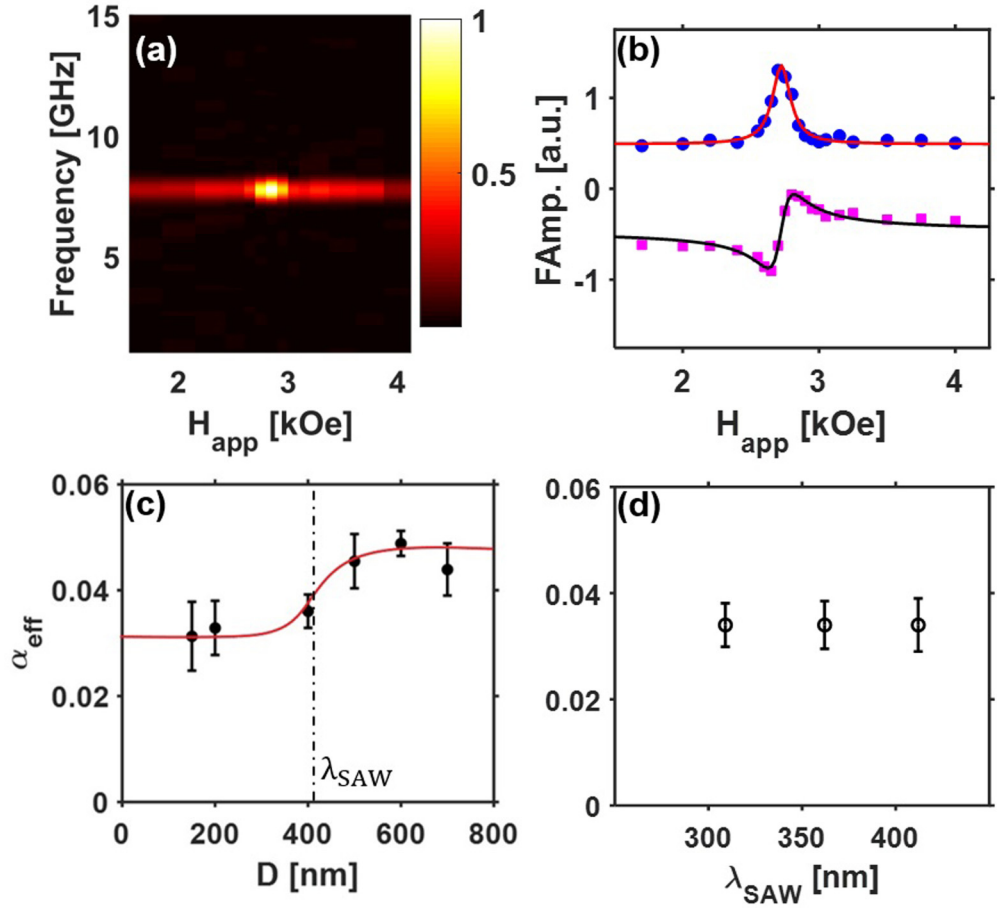


FIG. 3. (a) An example of field-dependent absolute Fourier amplitude for the $D = 410$-nm nanomagnet driven by the 412-nm SAW. (b) Corresponding field dependence of the normalized complex Fourier spectra (imaginary Fourier component – circles, real Fourier component – squares) of the MEL-driven dynamics of the nanomagnet. (c) The effective damping of different nanomagnets driven by the 412-nm SAW; the line is a guide to the eye. (d) The effective damping of the 200-nm nanomagnet driven by different SAW wavelengths.

TABLE I. Summary of key material parameters used to model the elastic profile. Here, $E$ is Young's modulus, $\rho$ is the density, $\alpha_V$ is the coefficient of thermal expansion, and $R$ is the reflectance at the pump-pulse wavelength.

| Material | E (GPa) | $\rho$ (g/cm$^3$) | $\alpha_V$ ($\mu m$/m K) | $R$ (%) |
|---|---|---|---|---|
| Nickel | 200 | 8.9 | 13 | 51 |
| Aluminum | 72 | 2.7 | 22.5 | 92 |
| Hafnium oxide | 161 | 9.68 | 6 | 14 |
| Silicon | 185 | 2.329 | 2.6 | 48 |

10–300 GHz, could be used to efficiently excite spin dynamics in these devices.

To investigate the origin of the size-dependent precession amplitude and damping behavior of the magnetoelastic resonances, we performed magnetomechanical simulations using a previously described multstep approach [20,21]. First, the lattice temperatures of the photoexcited Al bars are determined using a two-temperature model implemented in the finite-element modeling software FREEFEM++. The simulated temperature is then used to calculate the thermal expansion of the periodically arranged bars, which subsequently form SAWs due to their periodic arrangement. All the relevant parameters for the elastic simulation are listed in Table I below.

The elastic profile is then used as an input into the Object-Oriented Micromagnetic Framework (OOMMF) with an appropriate magnetoelastic extension, oommf-mel, that calculates the spatially varying field ($H_{\mathrm{MEL}}$). Because our polar TR-MOKE setup is sensitive to changes in $m_z$, we extracted the amplitude of $m_z$ from the magnetoelastic calculations for various nanomagnet sizes [Fig. 4(a)]. We find that the amplitude increases exponentially with decreasing $D$, just as in the experiment. In Fig. 4(b), the oscillations of the 200- and 500-nm samples, respectively, are shown to highlight the distinct behavior of samples with lateral dimensions less than or greater than the SAW wavelength.

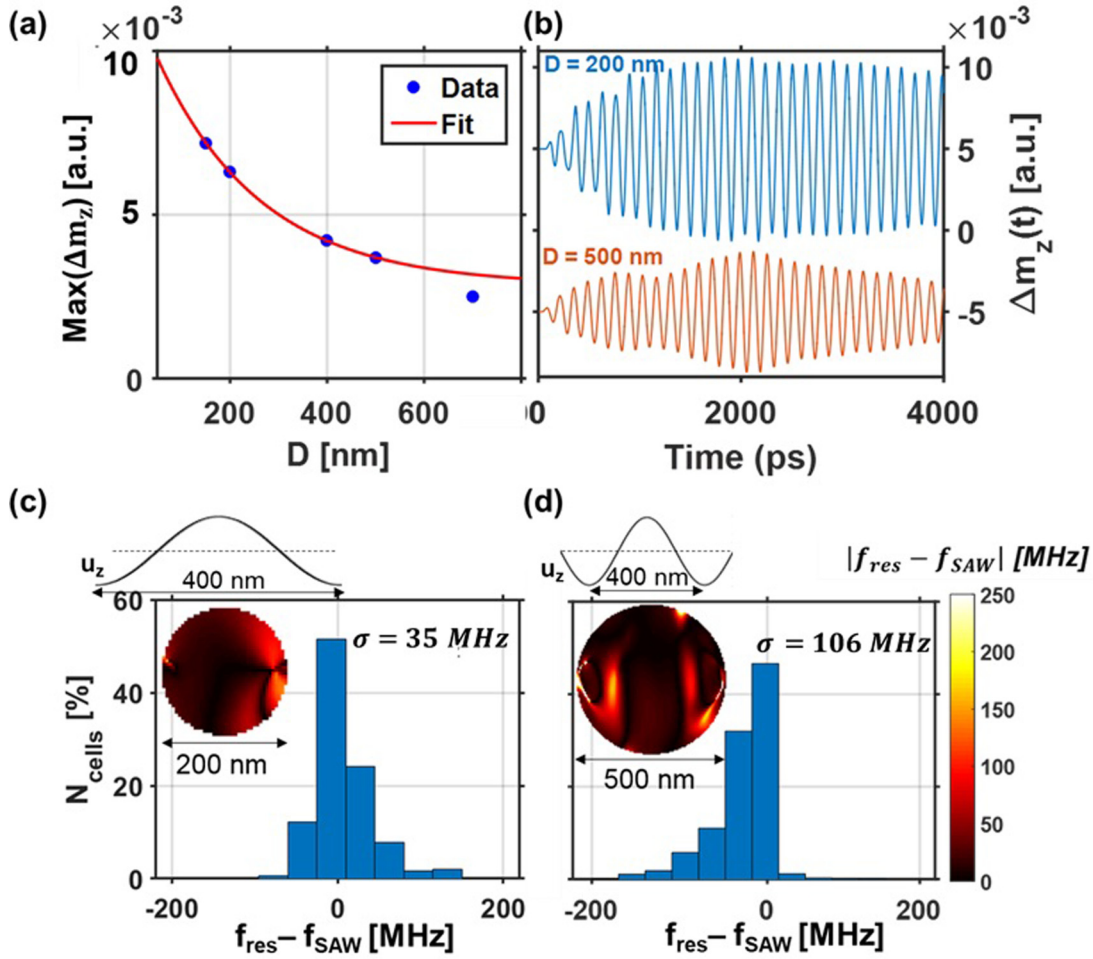


FIG. 4. (a) The maximum precession amplitudes of $m_z$ taken from micromagnetic calculations of SAW-driven ($\lambda_{\mathrm{SAW}} = 400$ nm) spin dynamics for various nanomagnet diameters reveal an exponential increase with decreasing $D$, just as was experimentally observed. In (b), the time evolution of $m_z$ is shown for the $D = 200$- and 500-nm nanomagnets, respectively, to show the distinct behavior of each sample at $H_{\mathrm{res}}$. In (c) and (d), the difference between $f_{\mathrm{SAW}}$ and the local resonance frequency ($f_{\mathrm{res}}$) of each cell in the simulation is plotted as a histogram to show that the resonance frequencies in the small sample are more tightly distributed; Inset: spatial distributions of $|f_{\mathrm{res}} - f_{\mathrm{SAW}}|$ for each sample which show that the magnetic resonance deviates most near the nodes of the standing wave which is shown by the illustration of the fundamental acoustic mode ($u_z$) above the mode profiles.

We now turn our attention to the damping behavior of the micromagnetic simulations to shed light on the experimental observations. Because the damping increased for nanomagnets larger than the SAW wavelength, it's likely that the spatial character of the acoustically driven ferromagnetic resonance is non-uniform which leads to dynamic dephasing and larger damping. To determine the extent of spatial inhomogeneity, the time evolution of each cell in the micromagnetic simulation along the vertical dimension was averaged and then converted the data to the frequency domain using an FFT algorithm Then, the highest-amplitude component of the spectra for each cell was identified in order to determine the spatial character of the magnetic resonance [$f_{res}(x, y)$]. In Fig. 4(c), a histogram of the difference between $f_{res}$ in each cell and the driving frequency ($f_{SAW} \sim 7.8$ GHz) shows that a majority of the cells in the smaller sample are on resonance with $f_{SAW}$. For the larger sample [Fig. 4(d)], the same analysis shows the frequencies are more widely distributed. In the inset of each figure we show the spatial variation of $|f_{res} - f_{SAW}|$ for each sample as a surface plot, which reveals that the difference is largest close to the edges of the sample. The variance in $f_{res}$ leads to an increase in the field-swept linewidth and, therefore, $\alpha_{eff}$ per Eq. (2), as was experimentally observed. Using the standard deviations ($\sigma$) of the frequency distributions [Figs. 4(c) and 4(d)], we can estimate the increase in damping due to inhomogeneous broadening (IHB). We recall the following relationship between field-swept and frequency-swept linewidths, $\alpha = \gamma \Delta H/4\pi f = \Delta f/2f$, where the first fraction is simply Eq. (2) rearranged, and the second is the more general definition of the damping in terms of $\Delta f$, which is the FWHM of the frequency-swept linewidth [23]. The distribution of resonances in the nanomagnets will increase the effective linewidth ($\Delta f_{eff}$) as follows:

$$\alpha_{eff} = \frac{\Delta f_{eff}}{2f_{SAW}} = \frac{\Delta f + \Delta f_{IHB}}{2f_{SAW}} = \frac{2\alpha f_{SAW} + 2\sqrt{2\ln(2)}\sigma}{2f_{SAW}}, \tag{3}$$

where the term with the subscript IHB is the contribution stemming from the spatial variation in the resonance frequency. We have made use of the relationship between the FWHM and standard deviation of normal distributions, $\text{FWHM} = \Delta f_{IHB} = 2\sqrt{2\ln(2)}\sigma$. Per Eq. (3), the simulated frequency distribution corresponds to enhanced damping values of 0.036 and 0.047 for the 200- and 500-nm samples, respectively, which are remarkably close to the experimentally observed values of 0.034 and 0.046.

The larger mode inhomogeneity in the larger structure can be understood by considering the profile of the acoustic wave used to excite the spin dynamics. Because the counterpropagating SAWs form a standing wave, the nodes of the wave are located at fixed positions along the sample surface. Here, the nodes are at the edge of the 200-nm sample, whereas they are well inside the larger sample where the difference between $f_{res}$ and $f_{SAW}$ is largest [Figs. 4(c) and 4(d)]. It is worth noting that we have only considered the $z$ component of the displacement ($u_z$), because the amplitude of $u_z$ is more than double that of $u_x$. Although these components are out of phase and their nodes are, therefore, offset by $\lambda/4$ (100 nm here), the nanomagnets in this study have relatively small aspect ratios ($0.04 < \text{AR} < 0.2$) which means that the strain generated by $u_z$ is much larger than $u_x$. Per Ref. [21], $H_{MEL}$ is directly determined by the strain; hence, the dominant source of the magnetoelastic field driving the precession is the $z$ component of the mechanical wave. Lastly, we acknowledge that intralayer spin-current transport, which directly depends on the quantity $\boldsymbol{m} \times \nabla^2 \dot{\boldsymbol{m}}$, may also have contributed to the experimentally observed damping behavior [24–26]. Although exact quantification of this effect is beyond the scope of this study, our results show that SAWs can create highly localized resonances that could be utilized to further investigate this phenomenon.

## IV. CONCLUSION

In conclusion, we carried out size- and wavelength-dependent measurements of magnetization dynamics in nanostructures resonantly driven by SAWs. We show that the efficiency of the MEL resonance depends on the Gilbert damping as well as the relative nanomagnet size and acoustic wavelength. Magnetomechanical simulations show that inhomogeneous broadening of the elastically driven spin dynamics causes the enhanced damping observed for nanomagnets larger than the SAW wavelength. Conversely, our results suggest that the losses associated with acoustically driven spin dynamics scale favorably with nanomagnet dimensions. These findings provide a critical reference for the rational design of highly efficient nanoscale magnetoelastic devices operating at high frequencies.

## ACKNOWLEDGMENTS

This work was supported by the National Science Foundation under Grants No. ECCS-1509020 and No. DMR-1506104. We acknowledge T. Yuzvinsky and the W.M. Keck Center for Nanoscale Optofluidics at UC Santa Cruz.

[1] R. Skomski, J. Magn. Magn. Mater. **272–276**, 1476 (2004).
[2] Y. Huai, AAPPS Bulletin **18**(6), 33 (2008).
[3] A. Kikitsu, J. Magn. Magn. Mater. **321**, 526 (2009).
[4] H. J. Richter, A. Y. Dobin, O. Heinonen, K. Z. Gao, R. J. M. Veerdonk, R. T. Lynch, J. Xue, D. Weller, and S. Technology, IEEE Trans. Magn. **42**, 2255 (2006).
[5] A. Datta, D. Nathasingh, R. J. Martis, P. J. Flanders, and J. C. D. Graham, J. Appl. Phys. **55**, 1784 (1984).
[6] É. D. T. de Lacheisserie, *Magnetostriction: Theory and Applications of Magnetoelasticity* (CRC Press, Boca Raton, FL, 1993).
[7] E. Klokholm, IEEE Trans. Magn. **12**, 819 (1976).
[8] I. S. Camara, J. Y. Duquesne, A. Lemaître, C. Gourdon, and L. Thevenard, Phys. Rev. Appl. **11**, 014045 (2019).
[9] L. Thevenard, I. S. Camara, S. Majrab, M. Bernard, P. Rovillain, A. Lemaître, C. Gourdon, and J. Y. Duquesne, Phys. Rev. B **93**, 134430 (2016).

[10] P. Kuszewski, I. S. Camara, N. Biarrotte, L. Becerra, J. Von Bardeleben, W. Savero Torres, A. Lemaître, C. Gourdon, J. Y. Duquesne, and L. Thevenard, J. Phys.: Condens. Matter **30**, 244003 (2018).

[11] C. L. Chang, S. Mieszczak, M. Zelent, V. Besse, U. Martens, R. R. Tamming, J. Janusonis, P. Graczyk, M. Münzenberg, J. W. Kłos, and R. I. Tobey, Phys. Rev. Appl. **10**, 064051 (2018).

[12] A. K. Biswas, S. Bandyopadhyay, and J. Atulasimha, Appl. Phys. Lett. **103**, 232401 (2013).

[13] V. Sampath, N. D'Souza, D. Bhattacharya, G. M. Atkinson, S. Bandyopadhyay, and J. Atulasimha, Nano Lett. **16**, 5681 (2016).

[14] S. Mondal, M. A. Abeed, K. Dutta, A. De, S. Sahoo, A. Barman, and S. Bandyopadhyay, ACS Appl. Mater. Interf. **10**, 43970 (2018).

[15] C. Berk, M. Jaris, W. Yang, S. Dhuey, S. Cabrini, and H. Schmidt, Nat. Commun. **10**, 2652 (2019).

[16] W. G. Yang, M. Jaris, D. L. Hibbard-Lubow, C. Berk, and H. Schmidt, Phys. Rev. B **97**, 224410 (2018).

[17] N. Qureshi, S. Wang, M. A. Lowther, A. R. Hawkins, S. Kwon, A. Liddle, J. Bokor, and H. Schmidt, Nano Lett. **5**, 1413 (2005).

[18] A. Barman, S. Wang, J. D. Maas, A. R. Hawkins, S. Kwon, A. Liddle, J. Bokor, and H. Schmidt, Nano Lett. **6**, 2939 (2006).

[19] C. Berk, F. Ganss, M. Jaris, M. Albrecht, and H. Schmidt, Appl. Phys. Lett. **112**, 052401 (2018).

[20] M. Jaris, Y. Yahagi, B. K. Mahato, S. Dhuey, S. Cabrini, V. Nikitin, J. Stout, A. R. Hawkins, and H. Schmidt, Appl. Phys. Lett. **109**, 202403 (2016).

[21] Y. Yahagi, B. Harteneck, S. Cabrini, and H. Schmidt, Phys. Rev. B **90**, 140405(R) (2014).

[22] Y. Yahagi, C. R. Berk, B. D. Harteneck, S. D. Cabrini, and H. Schmidt, Appl. Phys. Lett. **104**, 162406 (2014).

[23] S. S. Kalarickal, P. Krivosik, M. Wu, C. E. Patton, M. L. Schneider, P. Kabos, T. J. Silva, and J. P. Nibarger, J. Appl. Phys. **99**, 093909 (2006).

[24] Y. Tserkovnyak, E. M. Hankiewicz, and G. Vignale, Phys. Rev. B **79**, 094415 (2009).

[25] Y. Li and W. E. Bailey, Phys. Rev. Lett. **116**, 117602 (2016).

[26] H. T. Nembach, J. M. Shaw, C. T. Boone, and T. J. Silva, Phys. Rev. Lett. **110**, 117201 (2013).